

The dynamics of heat lows over flat terrain

Thomas Spengler^{a*} and Roger K. Smith^b

^a*Institute for Atmospheric and Climate Science, ETH Zurich, Switzerland*

^b*Meteorological Institute, University of Munich, Germany*

ABSTRACT: The numerical model for a heat low developed by Rácz and Smith is extended to include a representation of radiative heating and cooling. The model is run with a higher horizontal resolution than the original version and is used to investigate additional dynamical aspects of the structure and evolution of a heat low over a subcontinental- or continental-scale circular island surrounded by sea. Of particular interest is the diurnal and day-to-day evolution of the upper- and lower-level circulations and the degree of balance that exists in these. The heat low is surmounted by an anticyclone, the development of which is closely tied to the outflow branch of the sea breeze. The anticyclone has a much smaller diurnal variation than the heat low and, unlike the heat low is largely in balance, except in the region affected by the upward-propagating gravity wave induced by the inland-penetrating sea breeze. There is a strong analogy to certain aspects of tropical cyclones, which have a warm core, a shallow unbalanced boundary layer, and which are surmounted also by an anticyclone. Principles governing the absolute angular momentum budget are the same as those relating to the tropical cyclones and to the zonal-mean flow over Antarctica. Implications of these principles for obtaining a realistic steady state in long-term integrations of axisymmetric models are discussed. Copyright © 2008 Royal Meteorological Society

KEY WORDS heat trough; thermal low; thermal trough; radiation scheme; balanced flow; angular momentum budget

Received 5 April 2008; Revised 10 September 2008; Accepted 8 October 2008

1. Introduction

Heat lows or heat troughs are prominent climatological features of many arid land areas of the world during the warmer months, especially at low latitudes where insolation is strong. These areas include northern and southwestern Africa, west Pakistan and northern India, the Qinghai-Xizang plateau in China, southwestern North America, Saudi Arabia, the Iberian Peninsula and north-western and northeastern Australia. A list of pertinent references is given by Rácz and Smith (1999, henceforth RS99). These systems are sometimes referred to as thermal lows or thermal troughs, respectively, and they are shallow disturbances, generally confined below 700 hPa. Heat lows and heat troughs have many dynamical features in common, the main difference being the more dominant role of horizontal deformation in the heat trough. The distinction in a surface isobaric chart can depend on the isobar spacing, where the former has at least one closed isobar while the latter has the form of an open wave. Both types of disturbance may be thought of as low-level cyclonic relative vorticity maxima that are linked to horizontal gradients of diabatic heating.

Over the last two and a half decades there have been several modelling studies of heat lows, some in idealized flow configurations (Leslie, 1980; Fandry and Leslie,

1984; Kepert and Smith, 1992; Gaertner *et al.*, 1993; Adams, 1986, 1993; RS99; Reichmann and Smith, 2003; Spengler *et al.*, 2005; Zängl and Chico, 2006) and others related to the heat low in specific regions (Leslie and Skinner, 1994; Alonso *et al.*, 1994; Portela and Castro, 1996; Hoinka and Castro, 2003).

RS99 investigated the evolution and structure of a heat low over a square area of flat land surrounded by sea, showing in particular the evolution of the relative vorticity and potential vorticity distributions. Their main findings may be summarized as follows:

- The heat low has a minimum surface pressure in the late afternoon or early evening following strong insolation of the land, while the relative vorticity is strongest in the early morning hours following a prolonged period of low-level convergence. Thus the heat low is not approximately in quasi-geostrophic balance.
- The low-level convergence is associated with the sea breeze and later with the nocturnal low-level jet.
- Although a cyclonic vortex, the heat low is characterized by an anticyclonic potential vorticity anomaly relative to its environment on account of the greatly reduced static stability in the convectively well-mixed boundary layer.
- As a result of the reduced static stability in the mixed layer, the horizontal components of relative vorticity and horizontal potential temperature

*Correspondence to: Thomas Spengler, Institute for Atmospheric and Climate Science, ETH Zurich, Universitätsstrasse 16, CH-8092 Zürich, Switzerland. E-mail: thomas.spengler@env.ethz.ch

gradient make a non-negligible contribution to the potential vorticity in certain flow regions.

RS99 investigated also the effects of differing sea area, land area and Coriolis parameter on various aspects of the heat low, but gave little attention to the overlying anticyclone. Nevertheless, the predictions of their model have been supported by recent observations of the Saharan heat low. They go some way also to explaining the observed diurnal cycle of the West African monsoon circulation (Parker *et al.*, 2005 and references) as well as that in the heat trough over northeastern Australia (e.g. Preissler *et al.*, 2002). In a subsequent paper, the two authors extended their model to examine the effects of orography on heat low formation and structure (Reichmann and Smith, 2003, henceforth RS03).

In the RS99 model, the cycle of diabatic heating and cooling of the atmosphere was accomplished using the Mellor–Yamada $2\frac{1}{4}$ parametrization scheme for the boundary layer (Mellor and Yamada, 1974) in association with surface heating or cooling. After long integration times, this scheme leads to unrealistic mixed-layer depths because the only mechanism for cooling to oppose the net heating of the atmosphere is that which occurs in a shallow layer adjacent to the surface. In an effort to remove this limitation, RS03 incorporated the radiation scheme proposed by Raymond (1994, henceforth R94) in the model. This scheme is based on a grey atmosphere approximation and allows the atmosphere to cool, thereby preventing the long-term growth of the mixed layer.

Recently, Spengler *et al.* (2005) extended the RS99 model to investigate the effects of simple basic flows on the dynamics of heat lows. During the course of that study, the first author discovered some errors in the model initialization and in the numerical implementation of the radiation scheme by RS03 and also errors in R94. The errors in the initialization were found to have a negligible effect on the results presented by RS03 and those made in the implementation of the radiation scheme had only a small impact.

In this paper we implement a corrected and extended version of the radiation scheme into a higher-resolution version of the RS99 model and describe some interesting new features of the solutions. In particular we investigate the structure and evolution of the anticyclonic circulation that forms above the heat low as well as the degree to which the flow is in balance. We plan to revisit the problem investigated by RS03 in a subsequent paper.

In section 2 we review briefly the model formulation, highlighting the differences from the original model. In particular, in subsection 3 we discuss the radiation scheme proposed by R94 with our correction and extension thereto. We begin in section 4 with a brief comparison of simulations with and without the radiation scheme and go on to describe the diurnal evolution of the heat low and the anticyclone above it during the mature stage of the calculation with the radiation scheme included. In that section we explore also the effects of different island radii and comment on the relation of the present calculations to those of RS99. In section 5 we investigate

the degree to which the flow is in gradient wind balance. Section 6 examines the spin-up of the heat low and upper anticyclone during the first six days of the calculation and section 7 considers briefly certain similarities of heat lows to tropical cyclones and the circulation above Antarctica. The conclusions are presented in section 8.

2. Model description

The numerical model is a modified version of the hydrostatic primitive-equation model described by RS99, the main changes being the implementation of a radiation scheme, a relaxation scheme for the horizontal boundary conditions, and ten additional upper model levels with increased horizontal diffusion to reduce reflection of gravity waves from the top of the domain. Other changes are those incorporated by Spengler *et al.* (2005), who used a bi-harmonic (∇^4) diffusion and higher horizontal resolution (25 km instead of 100 km) to provide an improved representation of the sea-breeze circulation. In contrast to RS99, we consider flow over a circular island instead of a square one, where the radius of the island is chosen to be 400, 800 or 1200 km. The additional degree of symmetry facilitates the application of angular momentum principles to interpret certain flow features.

The model is formulated in sigma-coordinates, (x, y, σ) , on a northern hemisphere f -plane centred at latitude 20°N (here $\sigma = p/p_s$, p is the pressure, and p_s the surface pressure). The equations are expressed as finite differences on a domain with 40 interior σ -levels. The latter are unequally spaced to provide a higher vertical resolution in the boundary layer. The vertical grid is staggered with the horizontal velocity components, geopotential, and temperature stored at σ -levels and the vertical σ velocity, $\dot{\sigma} = D\sigma/Dt$, stored half way between σ -levels. Here D/Dt is the material derivative. A non-staggered Arakawa A-Grid is used in the horizontal directions with all variables stored at each grid point. There are 199×199 grid points in the horizontal with a grid spacing of 25 km giving a total domain size 4950 km west to east and south to north. This size is larger than the 4000×4000 km square domain of interest and is chosen to minimize the influence of the boundaries on the solution.

2.1. Boundary conditions

Following the method proposed by Davies (1983), a relaxation scheme is applied as the horizontal boundary condition on the velocity components, temperature, and surface pressure. These fields are relaxed to the initial fields which correspond to a quiescent atmosphere in radiative equilibrium. At the upper boundary ($\sigma = 0$), $\dot{\sigma} = 0$. By itself, this condition would lead to the reflection of gravity waves at the top of the model domain. In order to reduce this reflection we increase the horizontal diffusion by a factor of 10 in the top ten model levels. The increase is linear with a $\log_{10} p$ profile from 7 hPa to 0.7 hPa. At the lower boundary ($\sigma = 1$), $\dot{\sigma} = 0$ and

Table I. Model parameters.

Parameter	Symbol	Value
Surface albedo	A	0.3
Specific heat of dry air at constant pressure	c_p	$1004.67 \text{ m}^2 \text{ s}^{-2} \text{ K}^{-1}$
Thickness of the first soil layer	D_1	7.2 cm
Thickness of the second soil layer	D_2	43.2 cm
Thickness of the third soil layer	D_3	43.2 cm
Coriolis parameter	f	$4.988 \times 10^{-5} \text{ s}^{-1}$
Solar constant	F_0	1365 W m^{-2}
Gravitational constant	g	9.806 m s^{-2}
von Kármán's constant	k	0.4
Diffusion parameter	K_0	$5 \times 10^{13} \text{ m}^4 \text{ s}^{-1}$
Reference pressure	p_0	1000 hPa
Specific gas constant for dry air	R	$287.04 \text{ m}^2 \text{ s}^{-1} \text{ K}^{-1}$
Sea-surface temperature	T_s	24 °C
Deep-soil temperature	T_{cl}	25 °C
Surface roughness length for momentum over land	z_{0l}	10 cm
Surface roughness length for momentum over sea	z_{0s}	1 cm
Surface roughness length for heat over land	z_{hl}	10
Surface roughness length for heat over sea	z_{hs}	4.5
Thermal emissivity	ε	0.98
Thermal conductivity	κ	$7.5 \times 10^{-7} \text{ m}^2 \text{ s}^{-1}$
Stefan–Boltzman constant	σ_{sb}	$5.67 \times 10^{-8} \text{ W m}^{-2} \text{ K}^{-4}$

the sea-surface temperature is held constant. Other conditions are specified by the boundary-layer formulation described in the appendix to RS99 and the formulation of diabatic processes which are considered next.

2.2. Diabatic processes

The temperature of the ground during many diurnal cycles of heating and cooling is diagnosed from a surface heat balance condition. For maximum simplicity, there is no moisture in the model. A heat diffusion equation is solved at three levels in the soil to compute the heat flux into or out of the ground. The surface parameters are detailed in Table I. The version of the scheme used has been verified by Tory (1997) against data for days 33 and 34 of the Wangara boundary-layer experiment (Clarke *et al.*, 1971).

3. Radiation scheme

The radiation scheme is a modified form of the simple scheme proposed by R94 for solar and long-wave radiative transfers. In this scheme, the atmosphere is assumed to radiate as a grey body in the infrared regime, i.e. there is no distinction in emission or absorption between different wavelengths in this regime. Absorption of solar radiation is based on a given profile adapted from Manabe and Strickler (1964), whereas the long-wave radiative transfer is calculated utilizing the Schwarzschild–Schuster approximation.

The equivalent potential temperature tendency is given by Equation (1) in R94, i.e.

$$\frac{d\theta_e}{dt} = L + \dot{R}, \quad (1)$$

where θ_e is the equivalent potential temperature, L represents a relaxation to a background state of the atmosphere, a term omitted in the present study, and \dot{R} represents the radiative heating rate given by

$$\dot{R} = \frac{\theta_e}{\rho c_p T} (Q_{\text{sol}} + Q_{\text{therm}}), \quad (2)$$

where Q_{sol} and Q_{therm} are the contributions due to the absorption of solar and long-wave radiation, respectively (Equation (8) in R94).

Since the present model does not include the effects of moisture, the equivalent potential temperature θ_e is simply replaced by the potential temperature θ in the above equations. In R94, Q_{sol} is given by

$$Q_{\text{sol}} = \epsilon \cos \alpha Q_{\text{max}} \exp \left\{ - \left(\frac{z - z_{\text{max}}}{z_w} \right)^2 \right\}, \quad (3)$$

where ϵ is a measure of the fraction of clear sky, $\cos(\alpha)$ is the cosine of the zenith angle of the sun and Q_{max} is the maximum heating rate, z_{max} is the (fixed) height of maximum heating and z_w is a fixed height. We use the same formula here with $\epsilon = 1$ because the model is dry. The units for Q_{max} given by R94 are K s^{-1} , which is not in accordance with Equation (2) where the units are W m^{-2} . The dimensionally correct form of the potential temperature tendency equation is

$$\frac{d\theta}{dt} = \dot{R} = \frac{\theta}{\rho c_p T} Q_{\text{therm}} + \frac{\theta}{T} Q_{\text{sol}}. \quad (4)$$

In contrast to R94, we include also a solar heating term in Q_{sol} to provide an idealized representation of radiative

Table II. Parameters used in Equation (5).

Parameter	Value
Q_{\max}^t	$3.5 \times 10^{-5} \text{ K s}^{-1} \approx 3 \text{ K day}^{-1}$
z_{\max}^t	$3 \times 10^3 \text{ m}$
z_w^t	$4 \times 10^3 \text{ m}$
Q_{\max}^s	$5 \times 10^{-4} \text{ K s}^{-1} \approx 43 \text{ K day}^{-1}$
z_{\max}^s	$5 \times 10^4 \text{ m}$
z_w^s	$1.8 \times 10^4 \text{ m}$

See text for definitions.

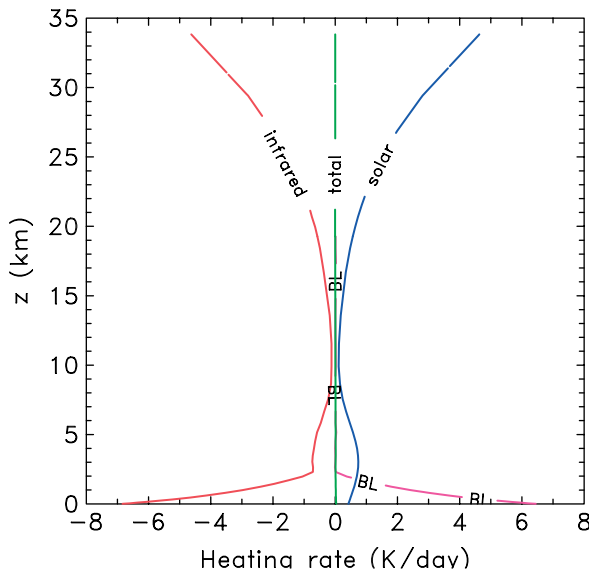


Figure 1. Vertical plot of daily integrated temperature tendencies in K day^{-1} . Labels indicate contributions from infrared, solar, boundary-layer parametrization (BL), and total. This figure is available in colour online at www.interscience.wiley.com/journal/qj

absorption by ozone in the stratosphere.

$$Q_{\text{sol}} = \epsilon \cos \alpha \left[Q_{\max}^t \exp \left\{ - \left(\frac{z - z_{\max}^t}{z_w^t} \right)^2 \right\} + Q_{\max}^s \exp \left\{ - \left(\frac{z - z_{\max}^s}{z_w^s} \right)^2 \right\} \right], \quad (5)$$

where t and s indicate the values corresponding to the troposphere or stratosphere, respectively. The temperature changes due to absorption of solar radiation with the parameters given in Table II produce heating rates (Figure 1) comparable to those of Manabe and Möller (1961) and London (1980) for an atmosphere in radiative equilibrium.

The values for Q_{\max} may appear rather large, but one must take into account the angle of the sun which enters through the $\cos \alpha$ term.

In a grey-atmosphere model for thermal radiation,

$$Q_{\text{therm}} = - \frac{d}{dz} (I^+ - I^-), \quad (6)$$

where I^+ and I^- are the upward and downward radiances. With the Schwarzschild–Schuster approximation,

these quantities are given by

$$\frac{dI^+}{dz} = \rho \mu (\sigma_{\text{sb}} T^4 - I^+), \quad (7)$$

and

$$\frac{dI^-}{dz} = - \rho \mu (\sigma_{\text{sb}} T^4 - I^-), \quad (8)$$

where μ is the effective absorptivity of the atmosphere in the infrared, and σ_{sb} is the Stefan–Boltzmann constant. Whereas R94 assumed μ to be constant, we prescribe a vertical variation to account for the higher concentration of water vapour in the lower troposphere, which is one of the main absorbing agents in the long-wave band. Specifically we take

$$\mu(z) = \mu_0 + \mu_1 \exp(-z/H), \quad (9)$$

where $H = 7000 \text{ m}$. $\mu_0 = 4.0 \times 10^{-4} \text{ m}^2 \text{ kg}^{-1}$ represents a background absorptivity and the second term, with $\mu_1 = 3.0 \times 10^{-4} \text{ m}^2 \text{ kg}^{-1}$, depicts the varying contribution from water vapour. Substituting Equations (7) and (8) into Equation (6) yields

$$Q_{\text{therm}} = - \rho \mu (2\sigma_{\text{sb}} T^4 - I^+ - I^-). \quad (10)$$

In Equation (9) in R94, the minus sign on the right-hand side of the corresponding equations (6) and (10) is missing. This omission leads to an incorrect sign for the temperature tendency in Equation (1). For example, a reduction of the upward radiance in a specific layer ($dI^+/dz < 0$) should cause an increase in temperature in the same layer ($d\theta/dt > 0$).

The lower boundary condition for I^+ allows for a radiative transfer from the ground into the first atmospheric model layer. Hence an upward radiative transfer can be calculated for the lowest atmospheric layer, as suggested by R94.

Since the proposed upper boundary condition, $I^- = 0$, at the top of the model domain in R94 results in strong heating above about 5 km in our calculations, we replace the condition $I^- = 0$ by $d\theta/dt = 0$ at the top of the domain, i.e. we assume radiative equilibrium. This assumption is motivated by the high degree of radiative balance in the mid-stratosphere. However, to apply this condition we need to define the temperature at the top of the domain, taken here to be 230 K at about 0.7 hPa.

4. Results

4.1. Impact of the radiation scheme

The impact of the new radiation scheme may be inferred from a comparison with a calculation without a radiation scheme in which the initial temperature sounding is chosen to be the same as for all the calculations presented here, i.e. a temperature profile which is in radiative

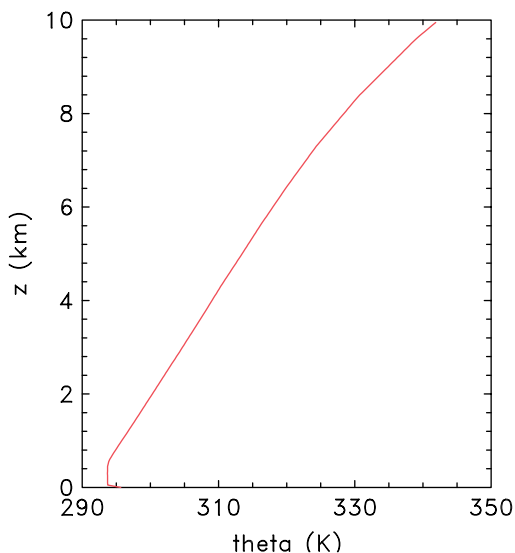


Figure 2. Initial vertical profile of potential temperature. This figure is available in colour online at www.interscience.wiley.com/journal/qj

equilibrium over sea (Figure 2). The impact is clear from the first four panels of Figure 3, which show vertical east–west cross-sections (subsequently referred to as height–radius cross-sections) of potential temperature and tangential wind speed in the late afternoon (1700 h) on day 11 in calculations with and without a radiation scheme. The time shown is in the late afternoon when the effects of insolation are near a maximum. The most striking difference in the potential temperature fields is the depth of the mixed layer as characterized by the depth of the region of uniform potential temperature at the centre of the domain. In the calculation without a radiation scheme, this depth is around 6 km, which is unrealistically large. With a radiation scheme, the depth is much more realistic at just over 4 km, a value that is typical of inland soundings across central Australia, for example (compare Figure 3(a, c)). The low-level winds are cyclonic and relatively light at this time, not exceeding 4 m s^{-1} with a radiation scheme and 6 m s^{-1} without one. The most striking feature of the azimuthal wind fields at 1700 h is the anticyclone, which has a maximum wind speed of over 12 m s^{-1} at heights between about 2 and 3 km in the case with a radiation scheme and a maximum of over 20 m s^{-1} at heights between about 3 and 4 km in the case without a radiation scheme. This anticyclone was not discussed by RS99, who focussed on the low-level cyclonic flow. Interestingly, this anticyclone extends throughout much of the troposphere, especially in the case with a radiation scheme, although it decreases in strength with height in the upper troposphere. This decay is consistent with slightly cooler air overlying the heat low, assuming thermal wind balance (cf. section 5).

4.2. Diurnal variation

Figures 3(e, f) show the height–radius cross-sections of potential temperature and tangential wind speed at 0500 h, a little before sunrise, on day 11 in the case

with a radiation scheme. By this day the flow has reached a mature stage with little variation from one diurnal cycle to the next, although without a radiation scheme the mean mixed-layer depth continues to increase slightly (not shown). Comparing these panels with the two above shows that at 0500 h, the low-level cyclonic circulation has increased markedly with the maximum wind speed exceeding 14 m s^{-1} , whereas in the case without a radiation scheme (not shown), the maximum just exceeds 18 m s^{-1} . In contrast the upper anticyclone exhibits relatively little diurnal variation, the maximum winds remaining approximately the same during the twelve hours to 1700 h.

We focus now on the mature stage of the calculation (day 11) *with* the radiation scheme. Figure 4 shows height–radius cross-sections of the radial velocity and vertical velocity components in the late afternoon (1700 h) and a little before sunrise (0500 h) in this stage. The most prominent features of the radial velocity at 1700 h (Figure 4(a)) are the shallow sea-breeze inflow near the coast and a weaker offshore component above the sea breeze extending to about 3 km in height. There is generally weak convergence over the land. The most prominent feature of the vertical velocity field at this time is the region of strong ascent near the sea-breeze front and the weaker subsidence offshore (Figure 4(b)). During the evening and early morning the sea breeze evolves into an even shallower nocturnal low-level jet that, by 0500 h, extends over much of the land area (Figure 4(c)). Unlike the sea breeze, the jet is not accompanied by significant vertical velocities at this time (Figure 4(d)).

The instantaneous fields shown in Figure 4 do not provide a very complete view of the diurnal evolution because the sea-breeze front initiates vertically propagating gravity waves. These are evident in high-temporal-resolution (10 min output) animations of the radial and vertical velocity fields. For this reason, instantaneous fields of the vertical velocity, in particular, cannot be interpreted in terms of buoyancy forcing on time-scales of many hours. (A discussion of the concept of buoyancy in vortical flows is given by Smith *et al.*, 2005.) The diurnal variability in these fields is similar to that in the spin-up phase and we defer a discussion of this aspect until section 6.

Figure 5 shows Hovmöller diagrams of the diurnal variation of radial velocity at the coast in the lowest 2 km on day 11 together with the potential temperature difference between 100 km inland and 100 km offshore. Above 1.3 km, outflow occurs during the entire day, whereas in the lowest 500 m there is inflow between 1300 h and 0600 h and outflow for the remainder of the day. The potential temperature is larger over land, except in the late evening to mid-morning (2100 h – 0900 h), when it is lower at heights below 150 m on account of a shallow layer of surface-based cooling. Thus the coastal outflow evident in the morning cannot be attributed to a gravity-induced land breeze, since the vertical extents of the outflow layer and the denser air do not match. The resulting asymmetry in the depth and intensity of the sea

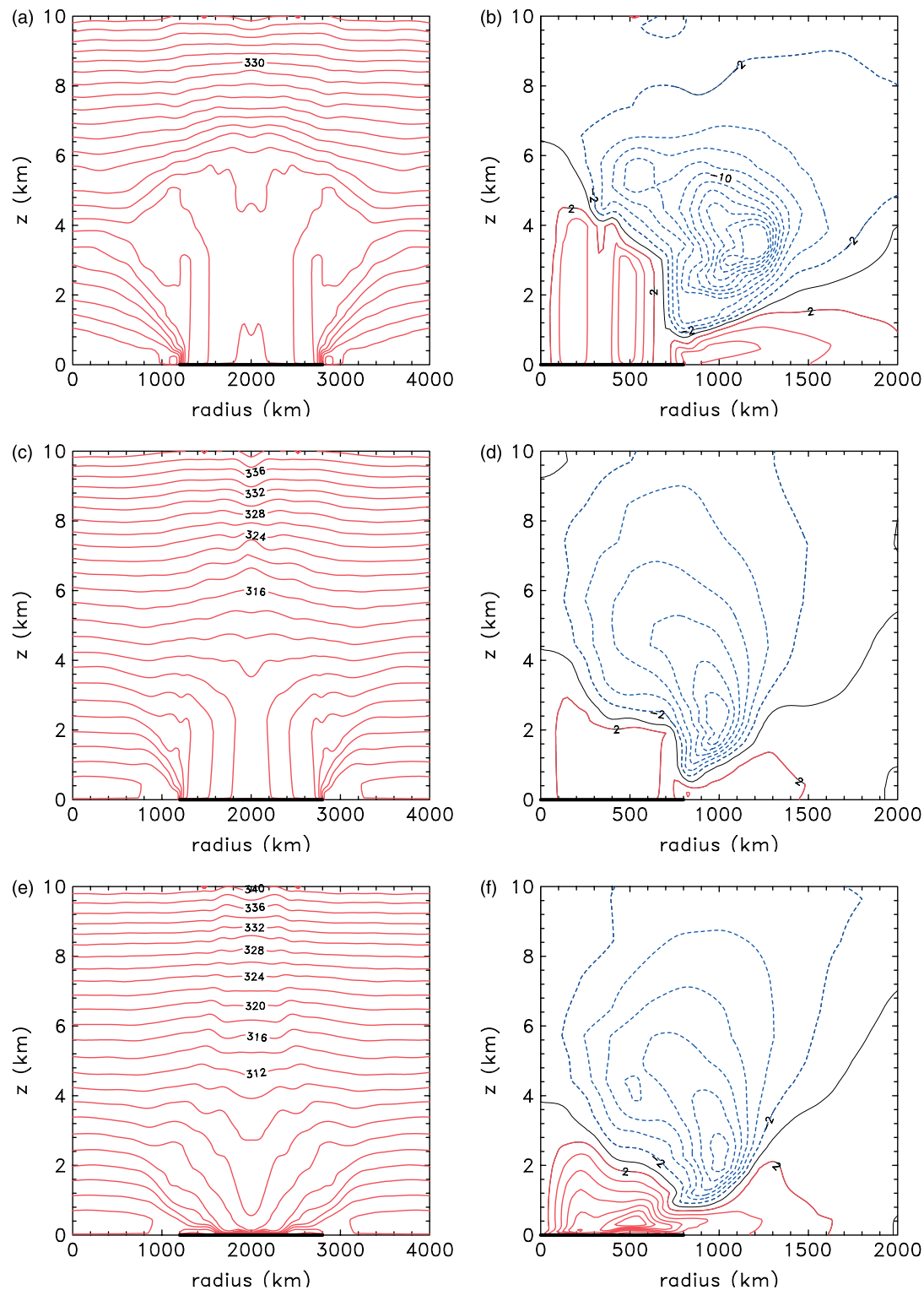


Figure 3. Height–radius cross-sections of (a) potential temperature (contour interval 2 K) and (b) the tangential wind component (contour interval 2 m s^{-1} ; solid lines indicate cyclonic and dashed lines anticyclonic circulation) at 1700 h in the mature stage of the calculation (day 11) without a radiation scheme. (c) to (f) show the corresponding cross-sections for the calculation with the new radiation scheme: (c) and (d) at 1700 h, and (e) and (f) at 0500 h. Only half of the domain is shown in the case of the wind fields. The thick black line along the abscissa shows the region of land. This figure is available in colour online at www.interscience.wiley.com/journal/qj

and land breezes has been noted before by Mak and Walsh (1976), who related the asymmetry to the diurnal stability fluctuations and variations of turbulent diffusivity.

The representativeness of the tangential wind fields in Figure 3 is indicated in Figure 6, which shows

vertical height–radius cross-sections of the mean fields of the tangential wind component between midnight and 0600 h and between noon and 1800 h. The cross-section between midnight and 0600 h is similar to that at 0500 h (Figure 3(f)) and the one between 0600 h and noon

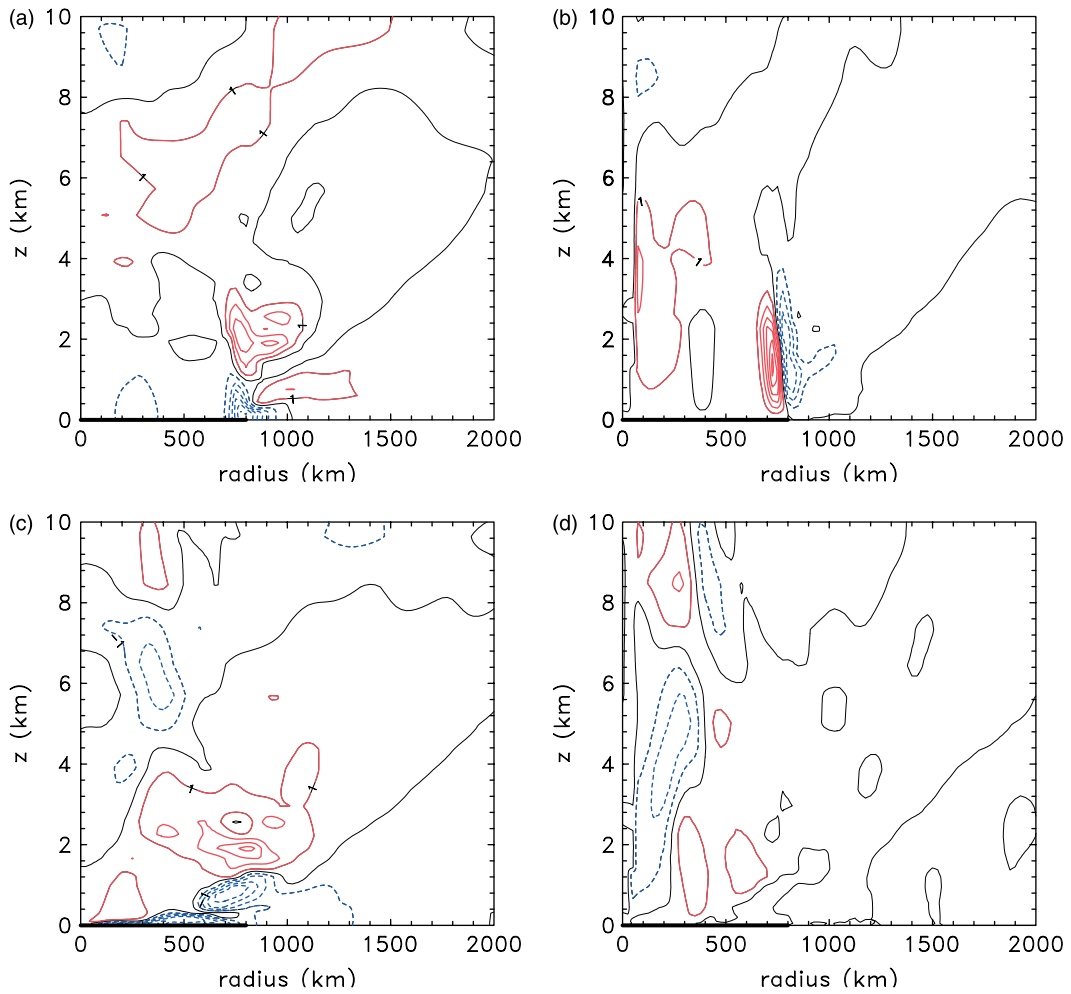


Figure 4. Height–radius cross-sections of (a) radial wind speed (contour interval 1 m s^{-1} ; solid lines indicate outward and dashed lines inward flow) and (b) the vertical velocity (contour interval 2 cm s^{-1} ; solid lines indicate upward and dashed lines downward flow) at 1700 h in the mature stage of the calculation (day 11) with the new radiation scheme. (c) and (d) show the corresponding cross-sections at 0500 h. The thick black line along the abscissa shows the region of land. This figure is available in colour online at www.interscience.wiley.com/journal/qj

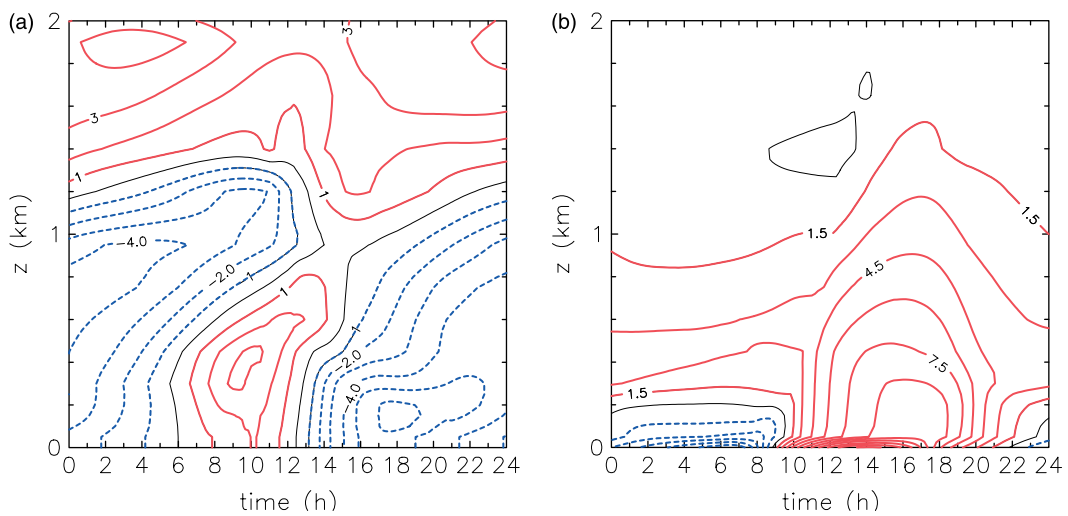


Figure 5. Height evolution (lowest 2 km) of (a) radial velocity at the coast line (contour interval 1 m s^{-1} ; solid lines indicate offshore and dashed lines onshore flow) and (b) difference of potential temperature between 100 km inland and 100 km offshore with time (contour interval 1.5 K). This figure is available in colour online at www.interscience.wiley.com/journal/qj

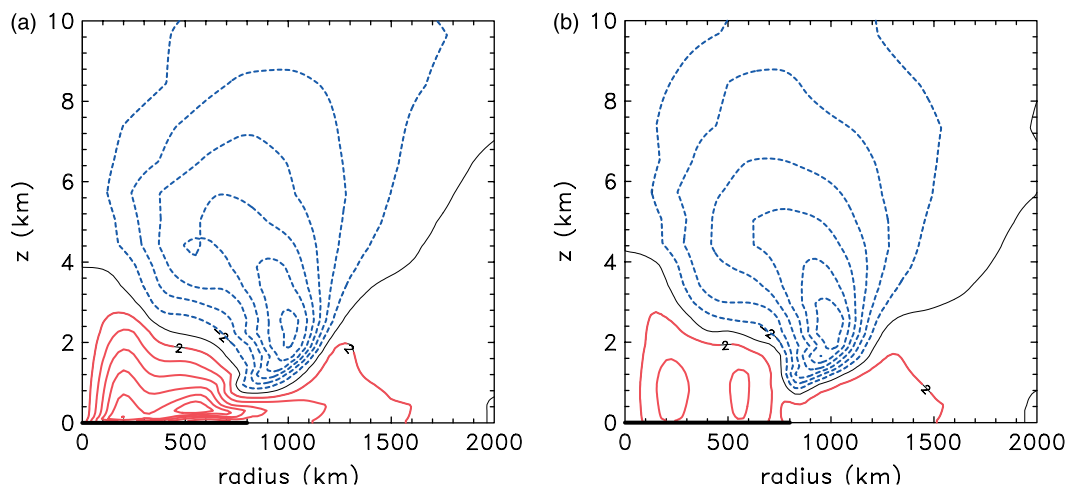


Figure 6. Height–radius cross-sections of the 6-hourly mean tangential wind component between (a) midnight and 0600 h and (b) noon and 1800 h in the mature stage of the calculation (day 11) with a radiation scheme. The contour interval is 2 m s^{-1} ; solid lines indicate cyclonic and dashed lines anticyclonic circulation. The thick black line along the abscissa shows the region of land. This figure is available in colour online at www.interscience.wiley.com/journal/qj

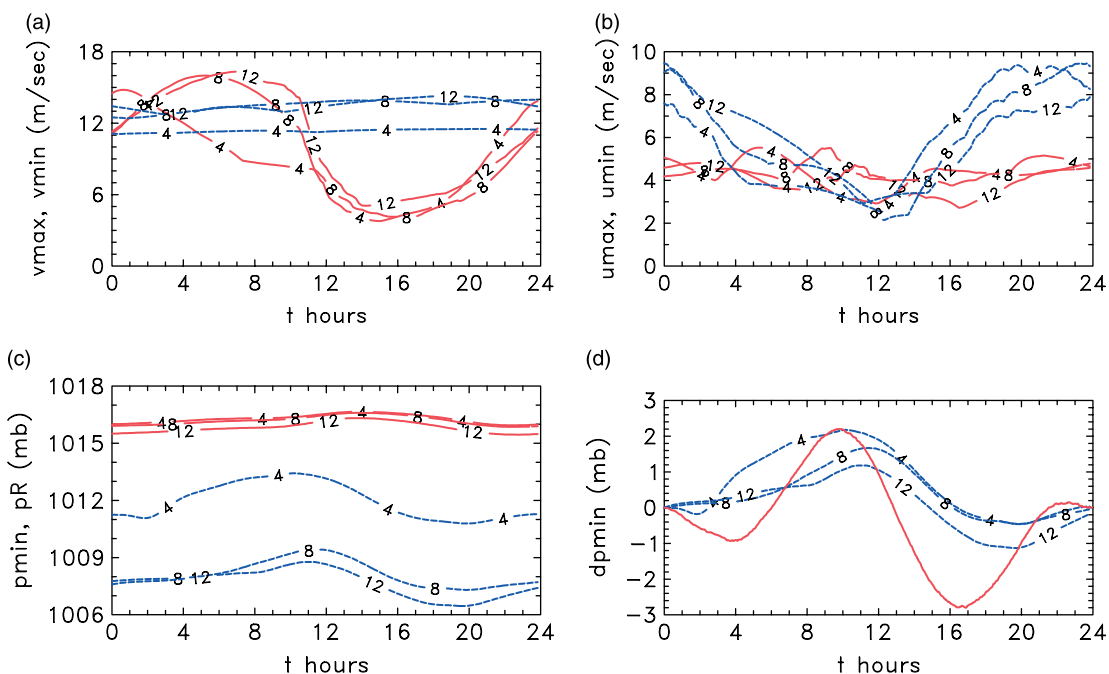


Figure 7. Time series of the magnitude of the maximum (solid curves) and minimum (dashed curves) (a) tangential velocity, v_{max} and v_{min} , and (b) radial velocity, u_{max} and u_{min} (all m s^{-1}). (c) shows minimum pressure, p_{min} (hPa) in the mature stage of the calculation (dashed curves), with 4, 8, and 12 referring to island radii of 400, 800 and 1200 km, respectively; the solid curves in (c) are the surface pressure at large radius, pR . (d) shows the diurnal variation of p_{min} in the calculations for different island radii compared with the observed mean variation (solid curve) at stations near 20°S over central Australia in September/October. This figure is available in colour online at www.interscience.wiley.com/journal/qj

(not shown) is only slightly different with the low-level cyclone being a little weaker in magnitude than in the early morning mean. Likewise, the cross-section between noon and 1800 h is similar to that at 1700 h (Figure 3(d)) and the one between 1800 h and midnight (not shown) is only slightly different with the low-level cyclone being a little stronger in magnitude than in the afternoon mean. Thus, in a mean sense we can distinguish between distinct patterns of the tangential flow component between midnight and noon, when the low-level cyclone is strongest, and between noon and midnight when it is much weaker. These differences

reflect the strong turbulent mixing of momentum in the mixed layer over land during the afternoon, which leads to a significant weakening of the cyclone, and the formation of a strong low-level jet at night, which re-amplifies the cyclone. In contrast, there is little diurnal variation in the mean strengths of the upper anticyclone during these periods.

Figure 7 summarizes the diurnal variation of the strength of the heat low, as determined by the maximum tangential wind speed, v_{max} , and the minimum surface pressure, p_{min} , and of strength of the upper-level anticyclone, as determined by the maximum anticyclonic wind

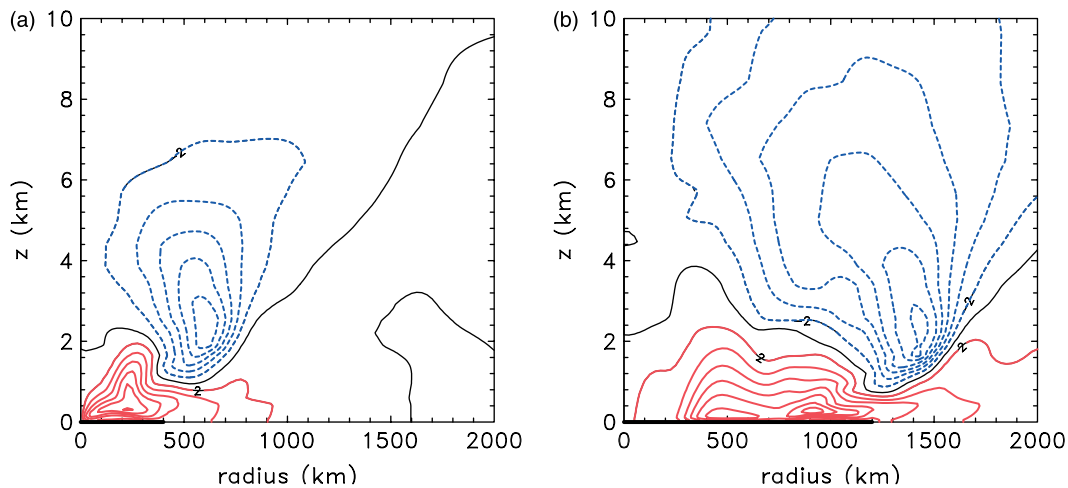


Figure 8. Height–radius cross-sections of the tangential wind component (contour interval 2 m s^{-1} ; solid lines indicate cyclonic and dashed lines anticyclonic circulation) at 0400 h in the mature stage of the calculation (day 11) for (a) the small island, and (b) the large island. The thick black line along the abscissa shows the region of land. This figure is available in colour online at www.interscience.wiley.com/journal/qj

speed, v_{min} (curves labelled 8, which refer to an island radius of 800 km). It shows also the variation in the strength of the meridional circulation, as measured by the strength of the maximum inflow, u_{min} , and outflow, u_{max} , and the surface pressure at the domain boundary, pR . While the minimum surface pressure occurs at 2000 h, the maximum tangential wind speed is attained between 0500 h and 0600 h and the minimum at 1600 h. Note that the diurnal range in v_{max} has an amplitude of 12 m s^{-1} . In contrast, the strength of the upper anticyclone shows no diurnal oscillation, although it increases slightly by 1.5 m s^{-1} during day 11, showing that the mature state on this day is still slowly evolving (section 7). The maximum value of p_{min} occurs just before noon, and the diurnal range of p_{min} is about 2 hPa. The pressure at large radius over the sea, pR , varies only slightly during the diurnal cycle.

4.3. Larger and smaller islands

It is of interest to know how the foregoing results depend on the size of the island. Therefore, in addition to the 800 km radius island considered so far, we repeated the calculations for island radii of 400 km and 1200 km, the latter being of continental scale such as Australia. Figure 7 shows the dependence of the parameters, v_{max} , v_{min} , u_{max} , u_{min} , p_{min} and pR on the size of the island. The most notable differences are between the smallest island and the others. The maximum tangential wind component during the afternoon is much weaker than in the other two and the diurnal mean pressure is higher by about 3 hPa. Nevertheless, the diurnal pressure variation is similar in all three cases.

Figure 7(d) compares the diurnal pressure variation for the three island radii with the mean observed variation at five surface stations between about 21°S and 24°S over central Australia obtained during a three-week period in September/October 1991 during the Central Australian Fronts Experiment (Smith *et al.*, 1995). It is interesting that the pressure variation in the calculation accounts for

at least half of the observed variation and the maximum occurs at about the same time, or one to two hours later, depending on the size of the island. On the other hand, it accounts for significantly less than half of the observed minimum and the minimum is about four hours later than that observed. That is not to suggest that the agreement with observations is poor, as the observed tidal variation is associated also with a gravity wave induced by the radiative heating of the upper atmosphere during the day and cooling during the night, a heating and cooling pattern that circles the globe once a day (e.g. Chapman and Lindzen, 1970). In our model, the heating and cooling pattern does not vary with longitude.

In the calculation for an island radius of 1200 km, the diurnal mean pressure is only slightly lower than that for an island radius of 800 km. The anticyclone is about 20% weaker in the case of the smaller island, but is similar in strength in the other two cases. The most apparent difference in the height–radius cross-sections (not shown) is that the sea breeze reaches the centre of the domain in the case of the smallest island, but not in the other two. In the larger island cases, the low-level tangential wind component has two maxima in the early morning, one associated with the decaying sea breeze and the other associated with the nocturnal low-level jet over the island, which develops independently provided there is a horizontal pressure gradient (Figure 8(b)). As the island size decreases, the separation between these two maxima decreases and for the smallest island there is only one maximum (Figure 8(a)).

4.4. Comparison with RS99

A quantitative comparison of the present calculations with those of RS99 is not warranted because here the environmental sounding is determined by the radiation scheme and is therefore different from that used by RS99. Furthermore, RS99 used a square island instead of the circular one used here. Because of the higher horizontal resolution and more selective horizontal diffusion in

the present model, the sea-breeze circulation is much more pronounced, otherwise the basic flow behaviour is similar in both models. The main calculation presented by RS99 had a land area of 600×600 km, comparable with the size of the Iberian Peninsula, providing the opportunity for the sea breezes to reach the domain centre by evening. This happens here only in the calculation with the land radius of 400 km. The RS99 calculation showed also an upper-level anticyclone, but its strength is somewhat weaker than in the main calculation analyzed here, consistent with the island size influence noted above (Figure 7(a)).

5. Balanced diagnostics

The relatively small diurnal variation in the upper-level anticyclone evident in Figure 3(d) and (f) and in Figure 7(a) suggests that this feature may be in close gradient wind balance. One consequence of balance would mean that the slow evolution of the vortex could be described using a Sawyer–Eliassen-type equation with the heating–cooling distribution determined by the radiative heating/cooling (e.g. Montgomery *et al.*, 2006 for the case of a tropical cyclone vortex). It would seem pertinent, therefore, to examine the balanced aspects of the flow in more detail. This problem is simplified here because the model is hydrostatic, ensuring that the flow evolves in hydrostatic balance. Thus any imbalance must reside in the radial momentum equation. It is of interest, therefore, to calculate the *net* radial force, i.e. the part of the radial pressure gradient force that is not balanced by the sum of the centrifugal and Coriolis forces. Vertical cross-sections of this quantity are shown in Figure 9. At 1700 h, the main regions of imbalance are associated with the sea-breeze flow and the low-level inflow over land. Other regions where the radial pressure gradient force deviates from its balanced value by more than 5 m s^{-2} are associated with gravity waves as indicated by animations of the fields at 10-minute intervals. At 0500 h, the main regions of

imbalance are associated with the low-level jet and with a vertically-propagating gravity wave located above the jet. Animations of vertical cross-sections of various quantities plotted at 10-minute intervals suggest that the lack of balance associated with the sea breeze is an important feature of the spin-up process.

6. Spin-up

The relative steadiness of the upper anticyclone and its deep vertical extent in the mature stage of the calculation raises interesting questions concerning its evolution. It is of interest also to examine the evolution of the heat low itself and the manner in which it spins up. Figure 10 shows the day-to-day variation of the quantities shown in Figure 7 for the first six days. Note that the maximum inflow increases slightly from day to day, a feature that is consistent with a gradual growth in the maximum temperature of the mixed layer. This increase is accompanied by a gradual increase in the maximum tangential wind speed and in the strength of the upper anticyclone, and a progressive decrease in the minimum surface pressure. On the other hand, the mean diurnal surface pressure at large radius shows little change. The maximum outflow does not change appreciably during the first six days.

To illustrate the spin-up of the heat low and the anticyclone above it, we show in Figure 11 vertical cross-sections of radial and tangential wind components at selected times 24 hours apart during the first three days of the calculation. The left panels show the pattern of inflow and outflow at 1800 h and the right panels show the tangential wind fields at midnight on each day. It is evident from these panels that the upper anticyclone is associated with the outflow branch of the sea breeze, since the maximum strength of the outflow occurs at the same height as the maximum anticyclonic flow. It is seen also that the vertical extent of the anticyclone over the land increases from day to day as the depth

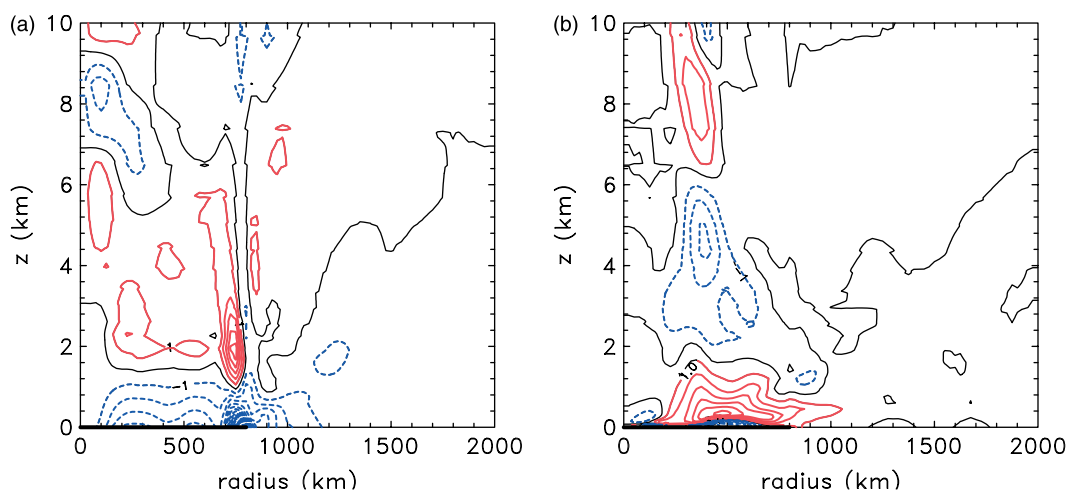


Figure 9. Height–radius cross-sections of unbalanced pressure gradient force per unit mass (contour interval $5 \times 10^{-5} \text{ m s}^{-2}$, solid lines indicate an outward- and dashed lines an inward-pressure gradient force) up to a height of 10 km at (a) 1700 h and (b) 0500 h. The thick black line along the abscissa shows the region of land. This figure is available in colour online at www.interscience.wiley.com/journal/qj

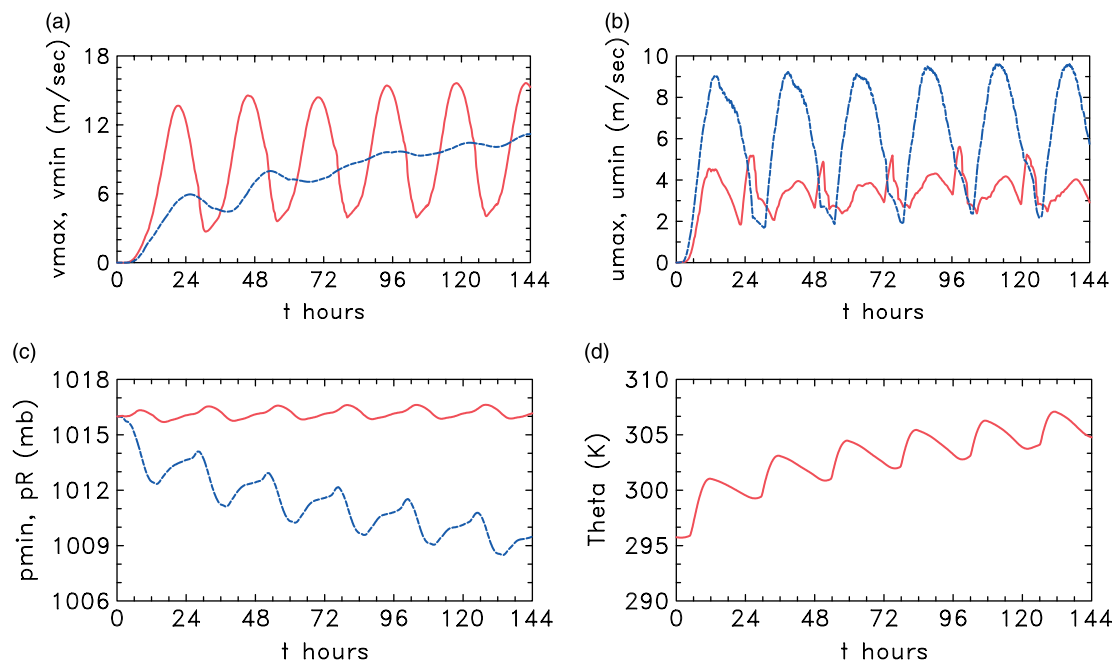


Figure 10. Time series of (a) v_{max} , v_{min} (m s^{-1}), (b) u_{max} , u_{min} (m s^{-1}), (c) p_{min} , pR (hPa), and (d) θ (K) at $r = 0$, $z = 1$ km, during the first six days of the calculation with the new radiation scheme. Dashed curves denote minimum values. This figure is available in colour online at www.interscience.wiley.com/journal/qj

of the outflow region above the heat low increases. Animations of the fields show this association more dramatically than the sequence of snapshots in Figure 11. They show also that the region of outflow has a significant diurnal variation, a feature that we investigate further below.

To understand why the anticyclone becomes progressively deeper it is instructive to examine the absolute angular momentum budget. The absolute angular momentum, M , is defined by

$$M = rv + \frac{1}{2}fr^2,$$

where r is the radius, v is the tangential wind speed, and f is the Coriolis parameter. For axisymmetric flow it satisfies the equation:

$$\frac{\partial M}{\partial t} + u \frac{\partial M}{\partial r} + w \frac{\partial M}{\partial z} = F, \quad (11)$$

where F is the frictional torque. For frictionless axisymmetric flow, M is conserved. Height–radius cross-sections of the terms in this equation at 0000 h on day 5 are shown in Figure 12. By far the largest contribution to the time tendency, $\partial M/\partial t$, is from the radial advection term $u(\partial M/\partial r)$, although the vertical advection $w(\partial M/\partial z)$ and the frictional term (estimated here as a residual) make a contribution below a height of 3 km, especially in the vicinity of the sea breeze. This result holds generally for all times and is associated with the fact that the radial gradient of absolute angular momentum is much larger than the vertical gradient, except possibly in the vicinity of the sea breeze. The radial advection term has a strong diurnal variation, which may be seen by comparing the time

tendency and the contribution to it from radial advection at 1200 h on day 5, shown in Figure 12(e) and (f), with those at 0000 h in (a) and (b). The variation is associated with a strong diurnal variation in the radial flow, which, in the middle and upper troposphere is intimately associated with the upward-propagating inertia-gravity wave initiated by the sea-breeze front. This gravity wave and its diurnal evolution are prominent features in the Hovmöller diagrams of vertical and radial velocities, even at a height of 8 km, as shown in Figure 13.

Figure 14 shows contours of absolute angular momentum at heights of 4 km and 8 km. At these altitudes, frictional effects are small and absolute angular momentum is approximately materially conserved. The oscillations evident in these contours are therefore indicative of air parcel motions, which are associated primarily with the oscillations in radial velocity shown in Figure 13. Note, however, that there is a small outward drift in the angular momentum contours. This drift is explained by the six-day mean radial outflow at these heights shown in Figure 15. This figure shows that the mean radial flow is positive at all heights above about 2 km over the land (even lower in the vicinity of the sea breeze). It is this persistent outward drift that accounts for the progressive deepening of the upper anticyclone because, as air parcels move outwards conserving their absolute angular momentum, they spin more slowly. The most plausible cause for the mean outward drift is a Stokes' drift associated with the inertia-gravity waves. Such a drift might be expected because friction at the land surface exerts a torque that depletes cyclonic relative angular momentum generated by the inflow. This depletion must be reflected in a progressive accumulation of anticyclonic relative angular momentum aloft and, in the absence of friction,

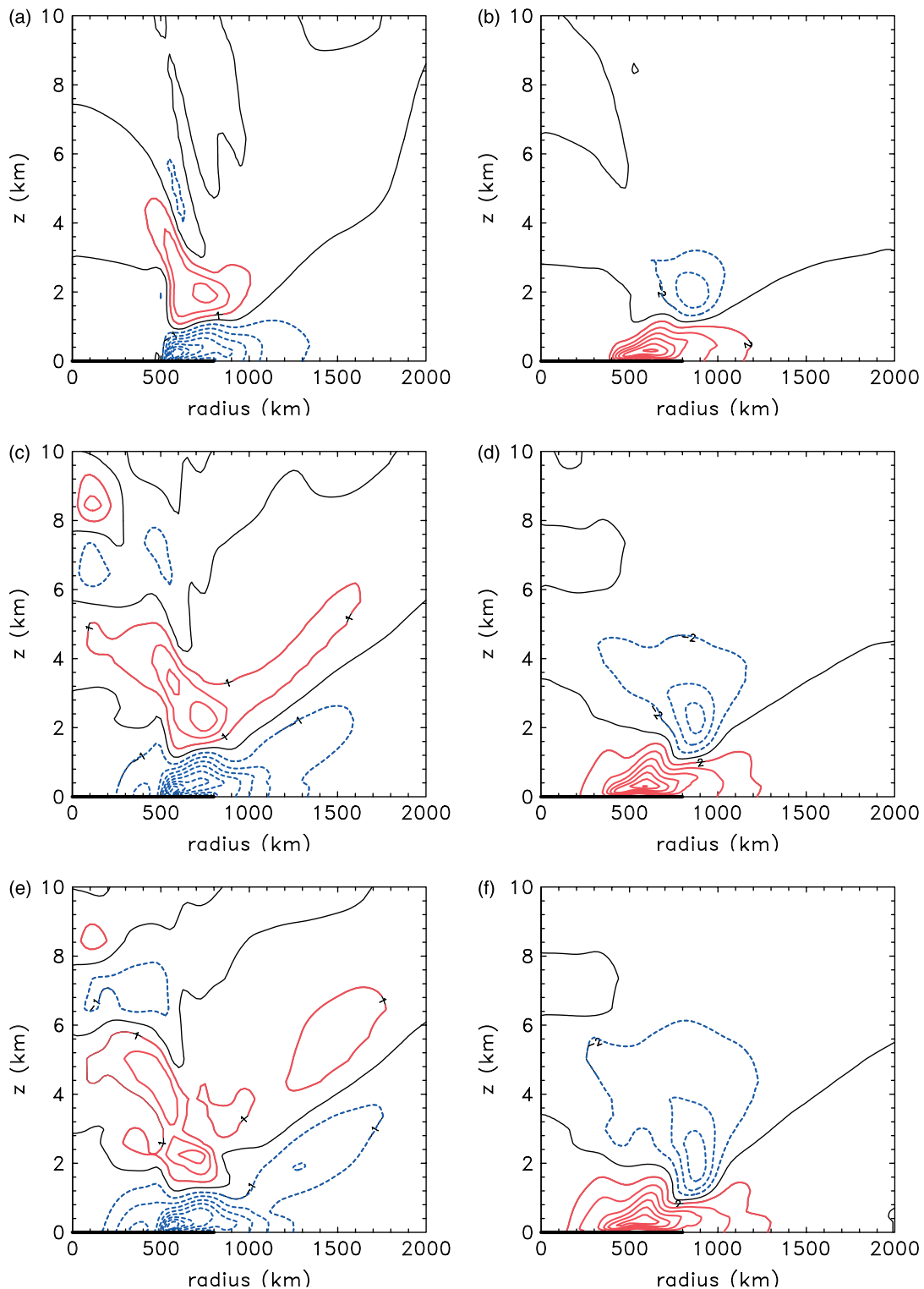


Figure 11. Height–radius cross-sections of the radial wind component (left panels; contour interval 2 m s^{-1} , with solid lines indicating outward and dashed lines inward flow) and tangential wind component (right panels; contour interval 2 m s^{-1} , with solid lines indicating cyclonic and dashed lines anticyclonic circulation) at selected times (a) 18 h, (b) 24 h, (c) 42 h, (d) 48 h, (e) 66 h and (f) 72 h during the first three days of the calculation with a radiation scheme. The thick black line along the abscissa shows the region of land. This figure is available in colour online at www.interscience.wiley.com/journal/qj

the only way this anticyclonic flow can materialize is by radial outflow. The depletion of cyclonic relative angular momentum has consequences for the ability of the flow to achieve a true steady state, as discussed in the next section.

7. Some analogies with tropical cyclones and the flow over Antarctica

Heat lows fall into the same class of warm-core vortices as tropical cyclones with the cyclonic circulation

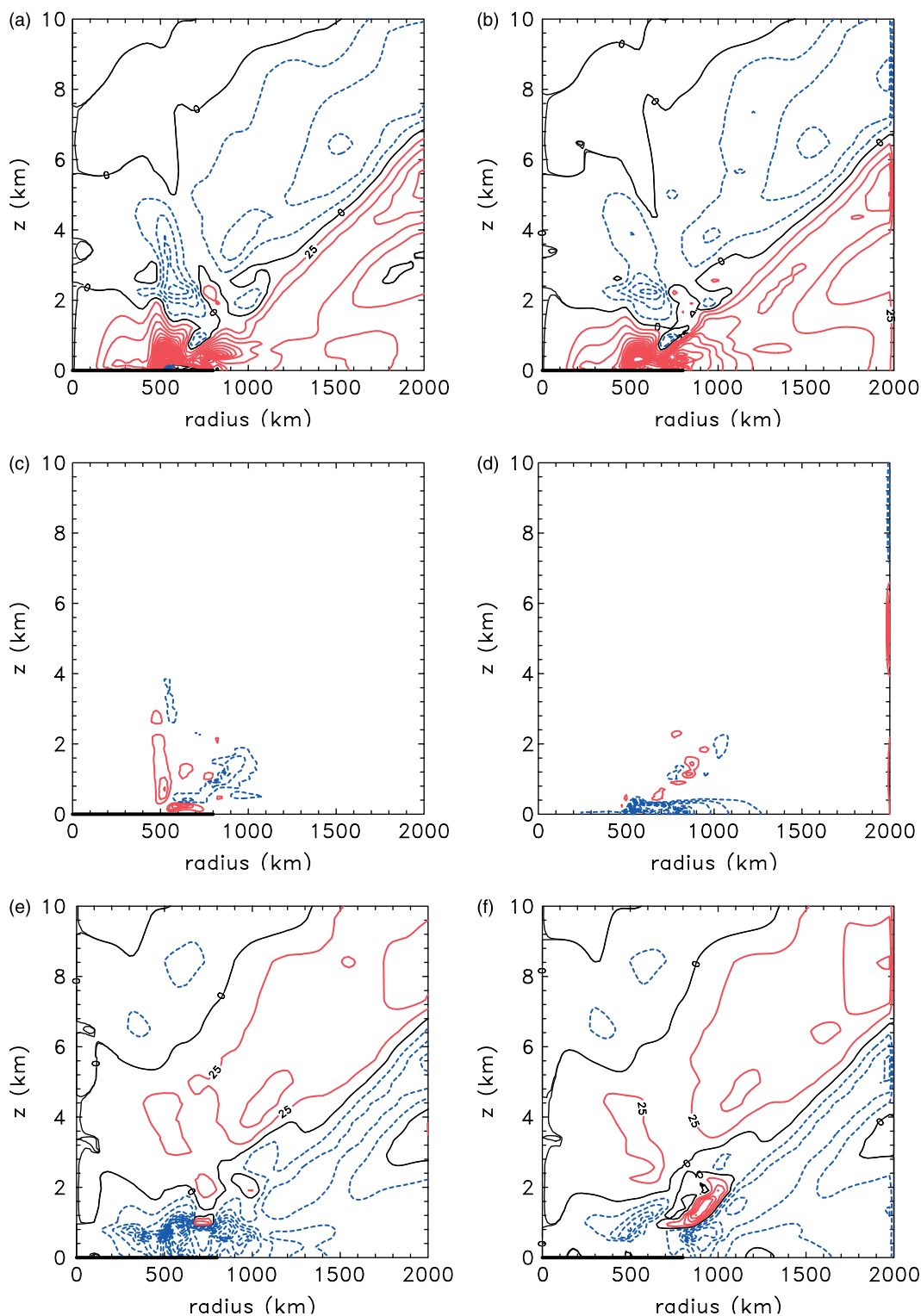


Figure 12. Height–radius cross-sections of (a) the absolute angular momentum tendency, and the contributions to this tendency from the (b) radial, and (c) vertical advection, at 0000 h on day 5. (d) shows the residual contribution, presumed to be associated with frictional effects. (e) and (f) are similar to (a) and (b), but for 1200 h on day 5 (contour interval $25 \text{ m}^2 \text{ s}^{-2}$; solid lines indicate gain and dashed lines loss of absolute angular momentum). The thick black line along the abscissa shows the region of land. This figure is available in colour online at www.interscience.wiley.com/journal/qj

being strongest at low levels and decaying with height, eventually becoming anticyclonic where the flow is radially outward. There are similarities also in the role of surface friction in the two types of vortices, each having strong inflow in a shallow boundary layer. In the heat low

case, the inflow is associated with the sea breeze and nocturnal low-level jet. The essential difference between the two types of vortices is the way in which the warm core is maintained: in the heat low it is primarily a result of diabatic heating in a deep, dry convective boundary layer,

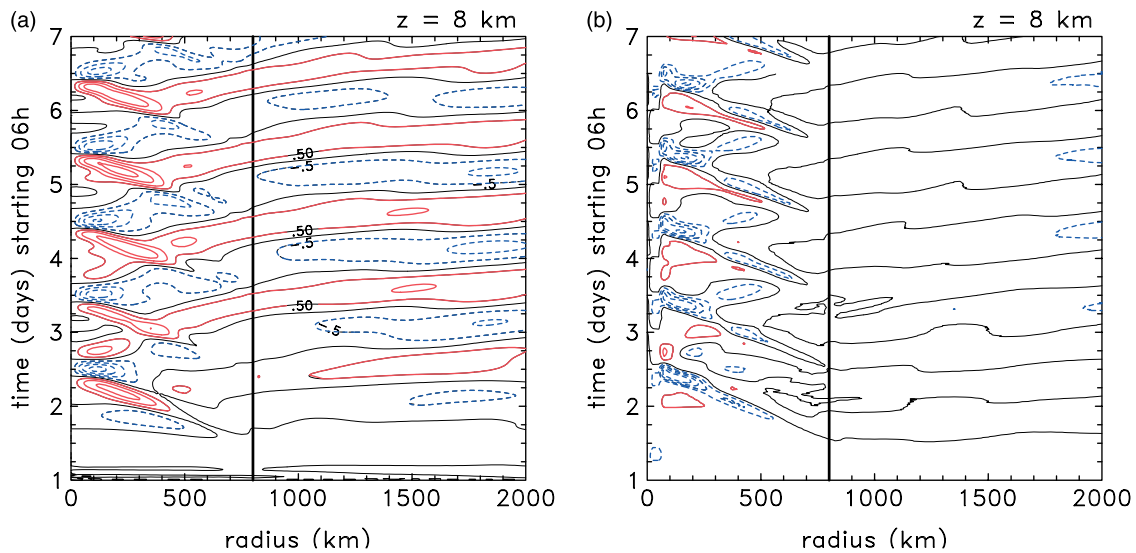


Figure 13. Hovmöller diagrams of (a) radial velocity, and (b) vertical velocity at a height of 8 km during the first six days of integration. The contour interval in (a) is 0.5 m s^{-1} , with solid lines indicating outward and dashed lines inward flow; the contour interval in (b) is 1 m s^{-1} , with solid lines indicating upward and dashed lines downward flow. The thick vertical line shows the position of the coast, with land to the left and sea to the right. This figure is available in colour online at www.interscience.wiley.com/journal/qj

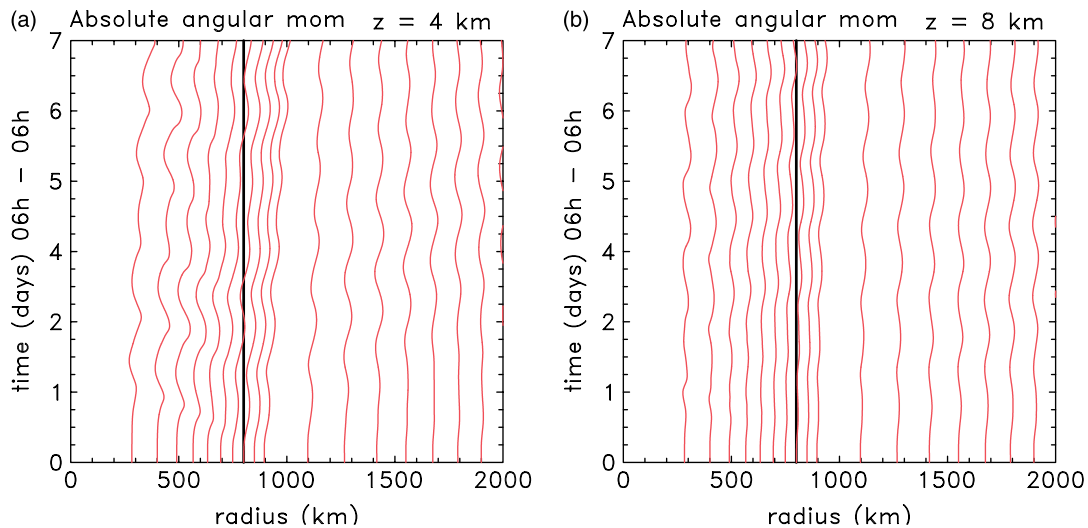


Figure 14. Hovmöller diagrams of absolute angular momentum at heights of (a) 4 km, and (b) 8 km during the first six days of integration. The contour interval is $2 \times 10^6 \text{ m}^2 \text{ s}^{-1}$ inside an initial radius of about 900 km and $2 \times 10^7 \text{ m}^2 \text{ s}^{-1}$ outside this radius. The thick vertical line shows the position of the coast, with land to the left and sea to the right. This figure is available in colour online at www.interscience.wiley.com/journal/qj

whereas in the tropical cyclone it is a result of moist deep convection in conjunction with enhanced surface moisture fluxes. Another conspicuous difference is that the frictional boundary layer in the heat low has a large diurnal component as a result of the strong diurnal variation of turbulent mixing over land.

Some of the fundamental principles involved in the dynamics of heat lows operate also in the airflow over Antarctica and it is informative to note these connections. The low-level flow over the ice slopes of the Antarctic plateau is dominated by katabatic drainage. The Coriolis forces acting on this drainage flow leads to zonal easterlies, i.e. to an anticyclonic circulation about the Pole. Likewise, the Coriolis forces acting on the return flow aloft lead to zonal westerlies, i.e. to an overlying cyclone. This is just a reversal of the situation in the heat low

or in a tropical cyclone, where the low-level circulation is cyclonic, the upper-level flow is anticyclonic and the (mean) meridional circulation is 'in, up and out'. (A simple model for the flow over Antarctica is described by Egger, 1985.)

In all three cases, absolute angular momentum is approximately conserved above the surface friction layer. In the case of the heat low and tropical cyclone, the surface torque leads to a sink of cyclonic angular momentum and, for a true steady state to exist, cyclonic angular momentum would have to be supplied to balance the surface loss. In the case of Antarctica, anticyclonic angular momentum is removed at the surface and in a steady state would have to be replenished somewhere in the flow. In all cases, the replenishment of the requisite angular momentum by axisymmetric processes alone is hard to

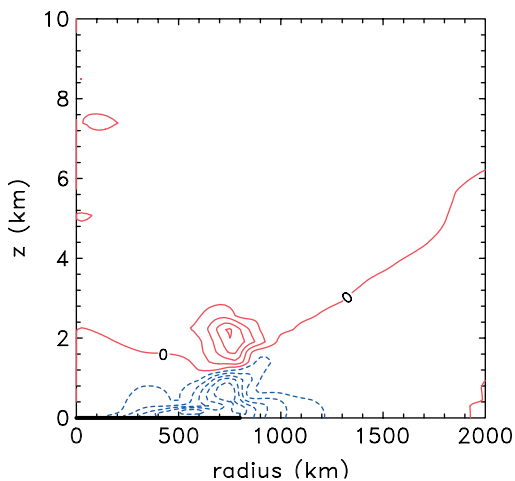


Figure 15. Height–radius cross-section of the mean radial wind component during the first six days of integration, starting at 0600 h on day 1. The contour interval is 0.5 m s^{-1} . The thick black line along the abscissa shows the region of land. This figure is available in colour online at www.interscience.wiley.com/journal/qj

imagine in reality and eddy fluxes must be undoubtedly invoked. Accordingly it may be surmised that any steady state that emerges in long-term integrations of these systems in axisymmetric models are unlikely to be realistic. Based on such considerations, Egger (1985) invokes eddy fluxes of westerly angular momentum at the edge of the Antarctic continent to account for the loss of easterly angular momentum at the surface of the ice slopes. To our knowledge, no authors have addressed this issue in detail in regard to tropical cyclones or heat lows. In the present model, which has rigid distant boundaries separated from the main flow region by a sponge layer, the replenishment of cyclonic angular momentum would have to come from lateral or vertical diffusion at boundaries where the flow adjacent to the boundary is anticyclonic. This mechanism is not realistic in the atmosphere. For this reason, our focus in this paper has been to understand the flow evolution during the first six days of integration and the quasi-steady state that emerges a few days later.

As discussed in section 6, the upper anticyclone exhibits a progressive upward extension as cyclonic relative angular momentum is depleted from the system by surface friction. The point at which this extension becomes unrealistic is a factor that remains to be determined, for example by suitable case-studies.

8. Conclusions

We have presented an improved numerical model for a heat low including a radiation scheme. The radiation scheme is a corrected and extended version of that proposed by Raymond (1994). Its implementation leads to a more realistic depth of the daytime mixed layer. We used the new model to investigate aspects of the dynamics of heat lows not previously touched upon including:

- the development of an upper-level anticyclone, and
- the degree to which the cyclonic and anticyclonic circulations are in gradient wind balance.

We showed that the upper-level anticyclone extends through much of the troposphere, but has its maximum strength in the lower troposphere, just offshore. It exhibits relatively little diurnal variation when the heat low reaches its mature stage; much less so than the low-level cyclone. The anticyclone develops steadily over a period of a few days and is associated with the return (offshore) branch of the sea-breeze circulation in the lower troposphere and a slow diurnal-mean outflow in the middle and upper troposphere. The outflow at upper levels may be interpreted as a mean drift induced by upward-propagating inertia-gravity waves that are initiated by the inland-penetrating sea-breeze front during the afternoon and evening.

Unlike the heat low, the upper anticyclone is largely in gradient wind balance, except in the neighbourhood of this gravity wave. The gravity wave has a significant effect on the radial and vertical components of the motion field at any one time and time averaging is required to isolate more thoroughly the steady-state structure of these components.

In a mean sense we can distinguish between distinct patterns of the tangential flow component

- between midnight and noon, when the low-level cyclone is strongest, and
- between noon and midnight when it is much weaker.

These differences reflect the strong turbulent mixing of momentum in the mixed layer over land during the afternoon, which leads to a significant weakening of the cyclone, and the formation of a strong low-level jet at night, which re-amplifies the cyclone circulation.

Finally we have drawn attention to certain dynamical similarities between heat lows and tropical cyclones. In particular we have shown that constraints imposed by the angular momentum budget are similar in both types of systems as well as in the problem of explaining the Zonal-mean flow over Antarctica. We discussed the implications of these constraints for obtaining a realistic steady state in long-term integrations of axisymmetric models.

Acknowledgements

We thank Michael Montgomery and Joe Egger for stimulating discussions about dynamical aspects of the paper and Günther Zängl and Jan Schween for their thoughts about some numerical and radiation issues, which helped to improve the paper. The authors are grateful also to the anonymous reviewers for their constructive criticism.

References

- Adams M. 1986. A theoretical study of the inland trough of northeastern Australia. *Austral. Meteorol. Mag.* **34**: 85–92.
- Adams M. 1993. A linear study of the effects of heating and orography on easterly airstreams with particular reference to northern Australia. *Austral. Meteorol. Mag.* **42**: 69–80.

- Alonso S, Portela A, Ramis C. 1994. First considerations on the structure and development of the Iberian thermal low-pressure system. *Ann. Geophys.* **12**: 457–468.
- Chapman S, Lindzen RS. 1970. *Atmospheric tides*. D. Reidel: Dordrecht, Netherlands.
- Clarke RH, Dyer AJ, Brook RR, Reid DG, Troup AJ. 1971. 'The Wangara experiment: Boundary-layer data'. Tech. Paper 19, Div. Meteorol. Phys., CSIRO: Aspendale, Australia.
- Davies HC. 1983. Limitations of some common lateral boundary schemes in regional NWP models. *Mon. Weather Rev.* **111**: 2013–2020.
- Egger J. 1985. Slope winds and the axisymmetric circulation over Antarctica. *J. Atmos. Sci.* **42**: 1859–1866.
- Fandry CB, Leslie LM. 1984. A two-layer quasi-geostrophic model of summer trough formation in the Australian subtropical easterlies. *J. Atmos. Sci.* **41**: 807–818.
- Gaertner MA, Fernandez C, Castro M. 1993. A two-dimensional simulation of the Iberian summer thermal low. *Mon. Weather Rev.* **121**: 2740–2756.
- Hoinka KP, Castro M. 2003. The Iberian peninsula thermal low. *Q. J. R. Meteorol. Soc.* **129**: 1491–1511.
- Keper JD, Smith RK. 1992. A simple model of the Australian west coast trough. *Mon. Weather Rev.* **120**: 2042–2055.
- Leslie LM. 1980. Numerical modeling of the summer heat low over Australia. *J. Appl. Meteorol.* **9**: 381–387.
- Leslie LM, Skinner TC. 1994. Real-time forecasting of the western Australian summertime trough: Evaluation of a new regional model. *Weather and Forecasting* **9**: 371–383.
- London J. 1980. Radiative energy sources and sinks in the stratosphere and mesosphere. Pp. 703–721 in Proceedings of the NATO Advanced Study Institute on Atmospheric Ozone, Aiken AC (ed.) Rep. No. FAA-EE-80-20, US Dept. of Transportation.
- Mak MK, Walsh JE. 1976. On the relative intensities of sea and land breezes. *J. Atmos. Sci.* **33**: 242–251.
- Manabe S, Strickler RF. 1964. Thermal equilibrium of the atmosphere with a convective adjustment. *J. Atmos. Sci.* **21**: 361–385.
- Manabe S, Möller F. 1961. On the radiative equilibrium and heat balance of the atmosphere. *Mon. Weather Rev.* **89**: 503–532.
- Mellor G, Yamada T. 1974. Hierarchy of turbulent closure models for planetary boundary layers. *J. Atmos. Sci.* **31**: 1791–1806.
- Montgomery MT, Nicholls ME, Cram TA, Saunders AB. 2006. A vortical hot tower route to tropical cyclogenesis. *J. Atmos. Sci.* **63**: 355–386.
- Parker DJ, Burton RR, Diongue-Niang A, Ellis RJ, Felton M, Taylor CM, Thorncroft CD, Bessemoulin P, Tomkins AM. 2005. The diurnal cycle of the West African Monsoon circulation. *Q. J. R. Meteorol. Soc.* **131**: 2839–2860.
- Portela A, Castro M. 1996. Summer thermal lows in the Iberian peninsula: A three-dimensional simulation. *Q. J. R. Meteorol. Soc.* **122**: 1–22.
- Preissler M, Reeder MJ, Smith RK. 2002. A case study of a heat low over central Australia. *Austral. Meteorol. Mag.* **51**: 155–163.
- Rácz Z, Smith RK. 1999. The dynamics of heat lows. *Q. J. R. Meteorol. Soc.* **125**: 225–252.
- Raymond DJ. 1994. Convective processes and tropical atmospheric circulations. *Q. J. R. Meteorol. Soc.* **120**: 1431–1455.
- Reichmann Z, Smith RK. 2003. Terrain influences on the dynamics of heat lows. *Q. J. R. Meteorol. Soc.* **129**: 1779–1793.
- Smith RK, Reeder MJ, Tapper NJ, Christie DR. 1995. Central Australian cold fronts. *Mon. Weather Rev.* **123**: 19–38.
- Smith RK, Montgomery MT, Zhu H. 2005. Buoyancy in tropical cyclones and other rapidly rotating vortices. *Dyn. Atmos. Oceans* **40**: 189–208.
- Spengler T, Reeder MJ, Smith RK. 2005. The dynamics of heat lows in simple background flows. *Q. J. R. Meteorol. Soc.* **131**: 3147–3165.
- Tory K. 1997. 'The effect of the continental planetary boundary layer on the evolution of fronts'. PhD dissertation, Monash University, Melbourne, Australia.
- Zängl G, Chico SG. 2006. The thermal circulation of a grand plateau: Sensitivity to the height, width, and shape of the plateau. *Mon. Weather Rev.* **134**: 2581–2600.